# Improving mechanical ice protection systems with substrate shape optimization

Valérian Palanque, Alexis Marboeuf, Marc Budinger, Valérie Pommier-Budinger, Lokman Bennani

# Improving mechanical ice protection systems with substrate shape optimization

V. Palanque [a,b,*], A. Marbœuf [a], M. Budinger [c], V. Pommier-Budinger [a], L. Bennani [b]

[a] ISAE-SUPAERO, University of Toulouse, 10 Avenue Edouard Belin, 31400 Toulouse, France
[b] ONERA/DMPE, University of Toulouse, F-31055 Toulouse, France
[c] Institut Cl'ement Ader (ICA), University of Toulouse, INSA, ISAE-SUPAERO, MINES ALBI, UPS, CNRS, France

*Keywords:*
De-icing
Fracture
Electro-mechanical
Optimization
Topology

A B S T R A C T

Mechanical and electro-mechanical de-icing systems are low-energy ice protection solutions based on fracture mechanisms. It can, however, be difficult to obtain the protection of an entire surface due to the limited propagation of fractures for some mechanisms. This article shows how it is possible to reshape the substrate in order to favor the propagation of adhesive fracture at the ice/substrate interface. The first part of the paper introduces an analytical beam theory approach for running computations quickly, making it possible to achieve parametric optimization of the substrate thickness and maximize the propagation length. The optimization results were validated using FEM software and tests on an aluminum prototype. A second method is also studied in this paper, topology optimization is used on a 2D finite element model to minimize the substrate mass of the proposed solution and adhesive crack propagation is assessed in comparison with the mass impact. For different boundary conditions, propagation ranges can be increased by up to 150% with a mass increase limited to 50%. Using topology optimization, the additional mass could be reduced by >60% while maintaining the same performances.

## 1. Introduction and objectives

Icing occurs when an aircraft flies through clouds in which supercooled droplets are suspended. With the ambient air temperature below the freezing point, the droplets freeze when impinging on the aircraft surfaces. As a consequence, significant ice buildup can occur (Raj et al., 2020). This ice accretion changes the airfoil geometry, altering the wing's aerodynamic characteristics (loss of lift, increase in drag). Icing conditions also threaten aircraft's engines with uncontrolled ice shedding and with air intakes protection grids icing, inducing power loss and eventually, causing engine flame-out in the case of total obstruction (Vercillo et al., 2019). Conventional thermal ice protection systems, such as hot air bleed systems (Moir and Seabridge, 2011) or more recent electro-thermal (bleed less) types, do require high power supply (Meier and Scholz, n.d.; Shinkafi and Lawson, 2014). Mechanically based ice protection systems tend to consume less energy because they do not require the phase change (liquid, vapor) of the ice. Solutions based on inflatable rods (pneumatic boots) (Ely and Macarchenia, n.d.), used e.g. on ATR regional aircraft, have a short lifetime due to elastomer material endurance. The electro-expulse types (Cox & Co company) (Ingram et al., n.d.) are efficient for metallic support but require large power supply and especially heavy supply capacitors. This paper focuses on an electro-mechanical resonant solution for airfoil structures such as leading edges, rotor blades or even wind turbines (Parent and Ilinca, 2011). Mechanical de-icing is achieved by applying significant stress to the ice. Upon reaching high stress intensities, failure of the ice occurs, initiating fractures in the material and eventually; leading to its shedding. This is done by deforming the skin covered by ice. Using resonance reduces the force required to deform the structure by matching with its modal frequencies. In (Budinger et al., 2018), Budinger et al. identified two types of resonant modes that can be used for electro-mechanical de-icing. Flexural modes, for which the power consumption is low but the protected area is limited, and extension modes, for which the protected area is extended but at the cost of higher power.

To efficiently realize mechanical de-icing, it is of utmost interest to understand the initiation and propagation of the fractures. Many studies were conducted to understand ice fracture propagation mechanisms. A combination of Cohesive Zone Model (CZM) and shear stress criterion were used to study numerically the bulk ice failure process on thin plates (Sommerwerk and Horst, 2017) and leading edges (Sommerwerk et al., 2020). In Shi et al. (2020), CZM was introduced to describe the interface

* Corresponding author at: ISAE-SUPAERO, University of Toulouse, 10 Avenue Edouard Belin, 31400 Toulouse, France.
*E-mail address:* valerian.palanque@isae-supaero.fr (V. Palanque).

https://doi.org/10.1016/j.coldregions.2022.103641

**Nomenclature**

| | |
|---|---|
| $\epsilon$ | Strain |
| $\omega_e$ | Strain energy density [J.m$^{-2}$] |
| $\sigma$ | Stress [kg.m$^{-1}$.s$^{-2}$] |
| $\sigma adm$ | Allowable tensile stress [kg.m$^{-1}$.s$^{-2}$] |
| $\sigma max$ | Maximum stress[J.m$^{-2}$] |
| $\sigma xx$ | Normal stress according to x direction [J.m$^{-2}$] |
| $b$ | Width of the sample [m] |
| $E$ | Young's modulus [kg.m$^{-1}$.s$^{-2}$] |
| $F$ | Load force [kg.m$^{1}$.s$^{-2}$] |
| $G$ | Energy release rate [J.m$^{-2}$] |
| $G_c$ | Critical energy release rate [J.m$^{-2}$] |
| $I_{Gz}$ | Quadratic momentum according to z direction [m$^4$] |
| $M_0$ | Clamp torque [kg.m$^2$.s$^{-2}$] |
| $M_f$ | Bending moment [kg.m$^2$.s$^{-2}$] |
| $U$ | Energy [J] |
| $U_y$ | Vertical displacement [m] |
| $y$ | Vertical distance to the neutral line of the beam [m] |

behavior of the plate and ice layer. Marboeuf et al. proposed a model based on phase-field variational approach to fracture (Marbœuf et al., 2020), showing the advantage of not requiring the a priori knowledge of the fracture propagation path. In Budinger et al. (2018), the energy balance approach is used to study ice failure in modal analyses. This method is fast to compute and does not require the traction-separation mandatory for CZM. A coupled criterion (CC) was firstly introduced by Leguillon in the study of adhesively bonded joints (Leguillon, 2002) (Martin et al., 2016) to predict the effects that lead to the crack initiation. According to this method, fracture initiation must meet both energy release rate and stress criteria. Later, Golovin et al. (2019) evaluated the influence of these criteria to assess the adhesive fracture propagation, highlighting the existence of two distinct shedding mechanisms according to different ice layer dimensions, one being stress dominant (small iced surfaces) and one being dominated by energy release rate (larger iced surfaces).

The objective of this paper is to show that it is possible to extend the protected area of flexural modes by modifying the shape of the substrate, especially the substrate's thickness, to increase ice delamination. The article focuses on low-frequency deformations which can be created using piezoelectric ceramics actuators (Budinger et al., 2018; Villeneuve et al., n.d.-a; Villeneuve et al., 2020; Villeneuve et al., n.d.-b) or Langevin transducers as in (Budinger et al., 2016). In this article, various approaches are used to model mechanical de-icing. In section 2, a method based on previous works (Pommier-Budinger et al., 2018; Budinger et al., 2021; Palanque et al., 2021) is used to discuss ice delamination limits for substrates of constant thickness. In this paper, delamination is studied for a substrate fully covered with freezer ice in order to study the limits of the fracture mechanism and the potential area protected by flexural modes. Then, section 3 introduces a method to push back these limits by using a parametric optimization algorithm to design a substrate of non-uniform thickness using a simple analytical beam approach based on Euler-Bernoulli beam theory equations, as shown in Bauchau and Craig (2009). In section 4, the analytical beam model is validated by comparing results with 2D FEM simulations and experimental tests carried out on aluminum prototypes. Finally, section 5 uses topology optimization (Akl et al., 2009; Zargham et al., 2016; Niemann et al., 2010; Sigmund, 2001; Andreassen et al., 2011) in order to obtain more freedom in shaping the substrate profile and to reduce the mass of the potential solution.

## 2. De-icing mechanisms under bending loads

### 2.1. Study case and assumptions for modeling and computation

In the case of electro-mechanical de-icing systems, the airfoil is deformed through modal excitation. Depending on the mode shape, the structure can be decomposed into simpler entities e.g. plates, to facilitate the study of the de-icing phenomenon (Fig. 1).

The objective of the paper is to improve adhesive fracture propagation at the ice/substrate interface for de-icing purposes. This can be done by studying a substrate (metal plate) fully covered with ice. In the case of electro-mechanical resonant actuation, the mechanical load is defined by the frequency that induces a modal shape and its amplitude. If a flexural mode is excited, the assumption can be made that the overall shape of the mode can be divided into several elementary blocks having the modal shape of the first mode of bending under anti-symmetric conditions (which happen to be very close to pinned conditions) (Fig. 2). For the extreme blocks of the plate, the boundary conditions are defined by the real boundary conditions of the study case (free, pinned, or clamped). Using the Rayleigh hypothesis, the modal shape of the elementary block is assumed to be close to the deflection of a beam under the bending load. A static approach can therefore be used to study the phenomenon of adhesive fracture propagation (Fig. 3).

Lastly, in order to simplify computations, the ice/substrate plate model is reduced to a composite beam model to use simple analytical equations to model the problem. Two different boundary conditions are studied as they are the boundary conditions corresponding to concrete applications:

the clamped condition (where the skin is attached on the structure reinforcements) and the pinned condition (for nodes at higher frequency modes).

The numerical simulations are performed in this article for a 200

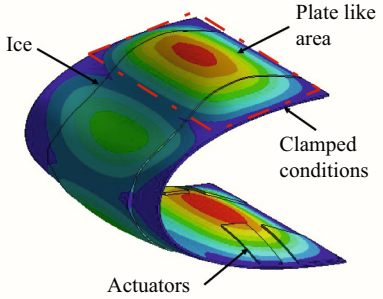


**Fig. 1.** Airfoil model under modal load.

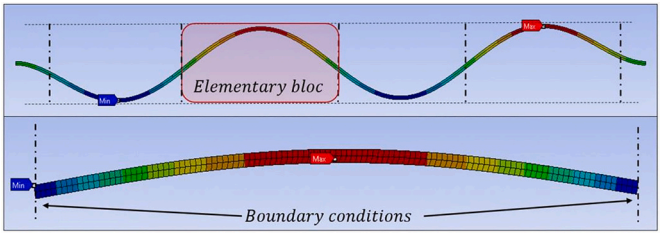


**Fig. 2.** Elementary block for studying flexural modes.

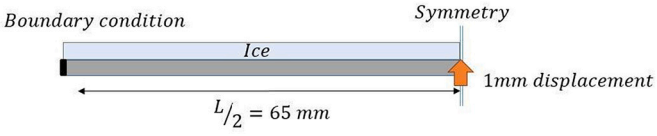


**Fig. 3.** Reduced static beam model used for computations.

mm-long, 40 mm-wide and 1.5 mm-thick (and sometimes also 2 mm-thick) aluminum substrate and a 1.5 mm-thick test sample is manufactured to validate the numerical results. Both ends of the sample are clamped, reducing the length of the substrate between the two clamps to 130 mm. A 2 mm-thick freezer ice layer is accreted over all the plate and is loaded under a three-point bending test condition by imposing a static displacement at the center of the sample on the side opposite the ice accretion.

### 2.2. De-icing mechanisms

In Budinger et al. (2021), fracture mechanisms for flexural modes are investigated. Following previous studies and experimental results, the mechanism under study (Fig. 4) is assumed to be divided into three steps that occur as the load amplitude increases:

- First, a cohesive fracture is initiated at the ice surface
- Then the cohesive fracture propagates through the ice to the interface
- Finally, upon reaching the interface, the crack pursues its propagation as an adhesive fracture along the ice/substrate interface.

As it is broadly done in the literature, the ice is here considered to be a brittle material (Tryde, 1980). Hence, to determine the location and the threshold of the crack initiation (first step of the fracture mechanism), the Rankine criterion is used. The Rankine criterion states that, when the principal stress exceeds the mechanical strength of a brittle material, failure occurs. In the case of brittle materials, there is no plastic deformation, therefore, at failure, crack initiation is observed. The tensile strength is considered as in the case of many brittle materials since it is much lower than the compressive strength. The tensile strength of the ice is in this article assumed to be around 3.0 MPa, which is a maximum value commonly used in the literature for freezer ice (Meng and Guo, n.d.; Petrovic, n.d.; Druez et al., 1986; Reich et al., 1994; Andrews and Lockington, 1983). After initiation, in most cases, the fracture instantaneously propagates to the interface thanks to the unstable behavior of the crack (second step of the fracture mechanism) (Palanque et al., 2021). This is explained using the Griffith theory on fracture propagation in brittle materials (Lawn, 1993; Anderson, 2005), which is detailed in the next part of the paper. Finally, the last step requires an increase of the load amplitude for adhesive propagation because of the crack's stable behavior (Budinger et al., 2021). As the total length of the ice block is significantly larger than its thickness in this case (beam configuration), it was shown in Golovin et.al work (Golovin et al., 2019) that the adhesive fracture mechanism is most likely dominated by energy release rate and that the interfacial shear stress is not the reason for the delamination. This theory was confirmed by finite element computations, showing a low shear stress level at the interface. However, this adhesive propagation is generally incomplete.

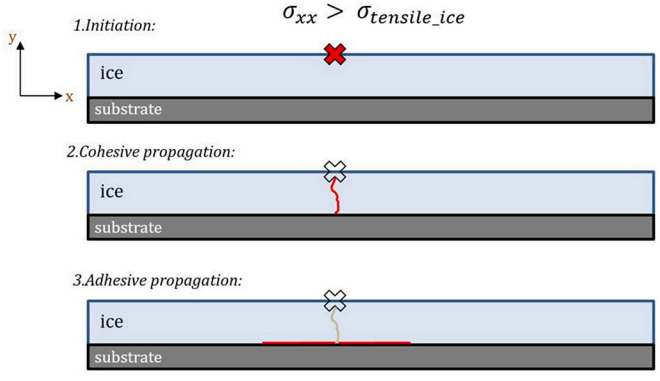


**Fig. 4.** Fracture mechanism for low-frequency flexural modes.

This paper focuses on the last part of the fracture mechanism, with the objective being to maximize ice delamination. Indeed, it has been shown in Palanque et al. (2021) that the early steps are much easier to complete and that the challenge is all about completing the last step as it is the main stumbling block to full ice shedding.

### 2.3. The Griffith theory and other efficiency criteria

The numerical study of fracture propagation can be done using Griffith's criterion (Zehnder, 2013), which compares the energy release rate of a structure $G$, of unit $[J/m^2]$, to a critical energy release rate $G_c$:

$$G = \frac{1}{b}\frac{dU}{dx} > G_c \tag{1}$$

where $b$ (in $[m]$) is the depth of the plate, $x$ (in $[m]$) the crack length and $U$ the strain energy (in $[J]$) in the structure.

This critical energy release rate can be characteristic of the intrinsic material properties (cohesive fracture) or of an interface adhesion (adhesive fracture).

A functional ice protection system must develop an energy release rate $G$ equal to or higher than $G_c$ over the entire surface to be protected to enable complete fracture propagation. However, the energy release rate is proportional to the strain energy $U$, which is proportional to the square of the load amplitude in linear elasticity. This means that increasing the amplitude will inevitably lead to exceeding the $G_c$ value as this will increase the energy release rate. To allow efficiency comparisons between configurations, (Budinger et al., 2021) proposes the use of design criteria independent of the load amplitude. For instance, as the elastic strain energy is proportional to the square of the strain magnitude and hence, to the square of the stresses, the ratio $G/\sigma_{max}^2$, with $\sigma_{max}$ the maximum mechanical stress of the substrate, is independent of the magnitude of the deformation. Comparing the ratio to the threshold $G_c/\sigma_{adm}^2$ is used to verify that the critical energy release rate value $G_c$ of the interface can be exceeded without having to exceed the allowable stress of the material $\sigma_{adm}$. Indeed, while the $G/\sigma_{max}^2$ ratio is greater than this threshold, reaching the right amplitude will enable the system to propagate the fractures over the surface without damaging the substrate.

### 2.4. Limit of mechanical de-icing on a uniform beam

Following previous arguments, this paper focuses on the study of the criterion $G/\sigma^2$ for different configurations to enable direct design comparisons. First, a uniform beam of constant thickness is studied for two different boundary conditions, clamped and pinned, to show the ice delamination limits. The clamped boundary condition is naturally encountered in aeronautical architectures where the metal skin of airfoils is riveted to the structure or glued in the case of composite material skin. A pinned condition can be obtained by a particular binding or deformation of the skin (in the case of multi-node deformation).

For this section, computations were made using the ANSYS static mechanical module. The displacement imposed for the numerical studies is of 1 mm at the center of the beam. The results, however, are independent of this displacement value using the previously introduced criterion. A 2D model is computed using the plain strain hypothesis. The size of the mesh and the number of elements according to the thickness (around 50,000 elements for the half model) were chosen after verifying the convergence of the results. In order to represent the propagation of the crack, different simulations are run with different crack lengths (Budinger et al., 2021). The crack area was first represented by a"contact without penetration" area, however, it was identified for long crack lengths that the computation time was very long or that the solver could not converge. Since the load is applied at slow rates, it was assumed that the kinetic energy in the de-bonded ice block is close to zero. Hence, since its strain energy is also close to zero, so the decision was made to

remove the ice block for which the adhesion was broken from the computation. This method was validated by checking, for relatively small cracks, that the results given by both methods were similar.

Figs. 5 and 6show the energy release rate for ice delamination computed for a beam in clamped and pinned conditions and for two thicknesses to analyze the influence of this parameter on the results. In the clamped case, after reaching zero, the criterion values goes up again, but this should not be taken into consideration as it is due to compressive stress. In the case of the computation of the energy release rate, the compression part must not be considered as it does not contribute to propagating the fracture (Marbœuf et al., 2020).

Figs. 5 and 6 show two important values: a theoretical propagation length and a practical propagation length. The theoretical propagation length represents the distance over which the fracture could propagate for an"infinite" load, i.e. the point at which $G$ goes down to zero. The theoretical propagation length is the maximum propagation length that can be reached without exceeding the mechanical strength of the substrate. The practical propagation length corresponds to the distance where the $G/\sigma_{max}^2$ value gets lower than the $G_c/\sigma_{adm}^2$ value. This means that it is possible to reach the practical length of propagation by increasing the load while being sure that the stress in the structure remains allowable. In our study with ice made in a freezer, the $G_c$ value is set to 1 $J/m^2$ as this is a value broadly used in the literature (Andrews and Lockington, 1983) for critical energy release rate of the adhesive interface with freezer ice. This value is of utmost important in the assessment of the fracture propagation and can be adapted in case of different ice such as atmospheric ice. The $\sigma_{adm}$ value is set to 50 MPa in order to ensure that the computation stays within the strain elastic domain as a 200 MPa mechanical strength is given by the aluminum supplier.

In this case, the important value to consider is the practical propagation length as it is the one used for comparisons with experimental studies. This value depends on the mechanical properties of the substrate and the critical energy release rate. For instance, the practical propagation length can be increased by upgrading the properties of the substrate using high resistance materials (high $\sigma_{adm}$) or low adhesion coatings (low $G_c$) (Golovin et al., 2019; Huang et al., 2019). It is impossible to exceed the theoretical value, however, which can therefore be used to assess the geometrical limits of the design.

The indicators show that the energy release rate is highly non-uniform over the fracture propagation length. It can be seen in particular that the clamped condition is unfavorable and limits the maximum de-icing capacities to 20% of the surface to be protected. The pinned boundary condition is more favorable, with a theoretical propagation length of 100%, however, the practical value is significantly lower because of a significant decrease in the $G$ value. The fact that, in the early stages of propagation, the $G$ values are relatively high and lead to an unnecessary propagation capacity is the motivation behind the next section's objective: optimize the energy distribution along the beam in order to extend the maximum propagation length. Computations show that the substrate thickness does not much influence the $G$ value. Therefore, for the rest of the paper, only a 1.5 mm substrate thickness will be considered.

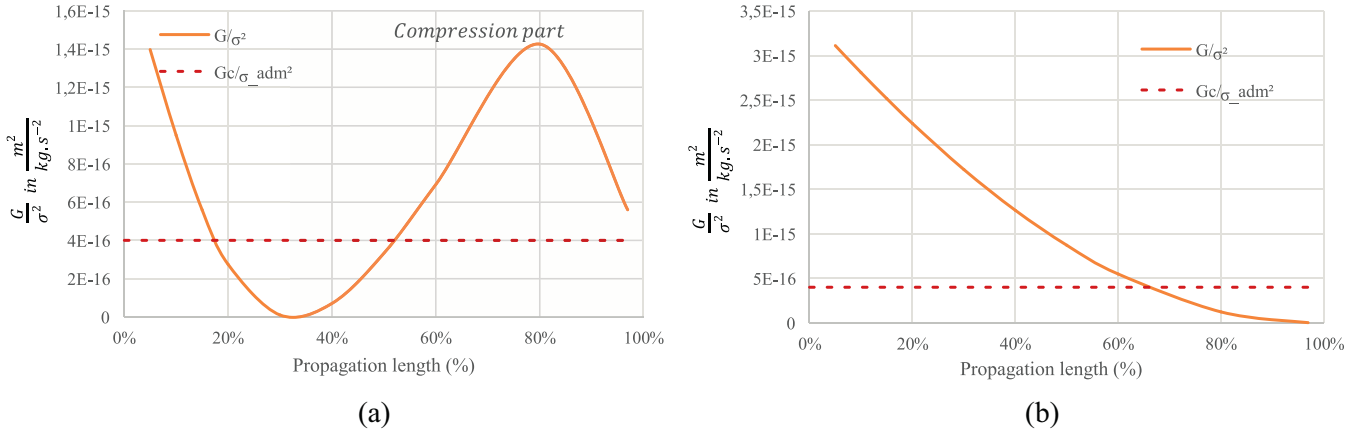


**Fig. 5.** Energy release rate for ice delamination over a 1.5 mm-thick aluminum clamped beam (a) and pinned beam (b).

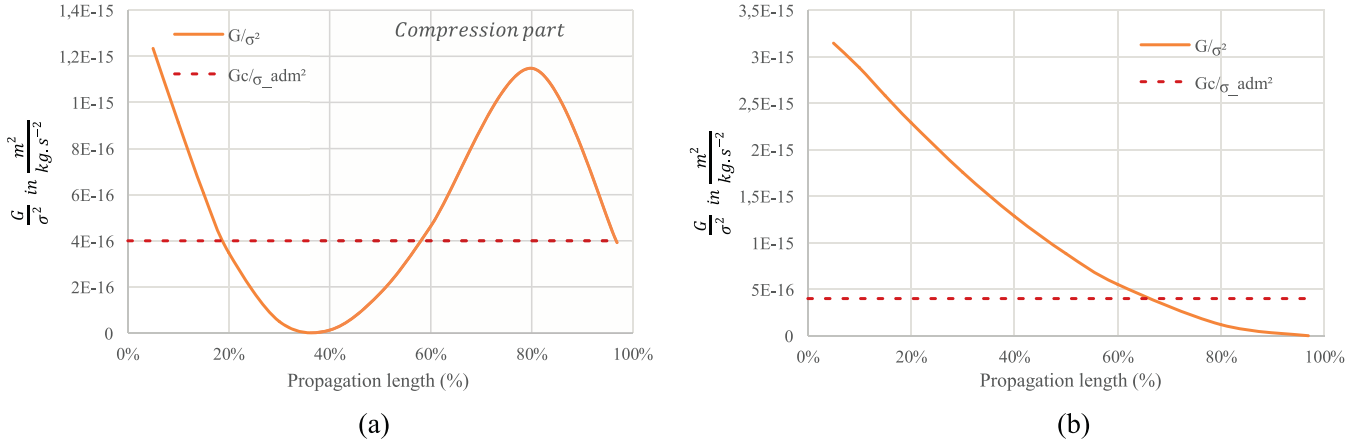


**Fig. 6.** Energy release rate for ice delamination over a 2 mm-thick aluminum clamped beam (a) and pinned beam (b).

## 3. Substrate thickness optimization

### 3.1. Non-uniform thickness motivation

In the case of a substrate with high stiffness (compared to the ice), it is acceptable to assume that the energy release rate is essentially due to the transfer of the energy contained in the ice which has lost its adhesion. The strain energy density in the ice is defined by:

$$w_e = \frac{1}{2}\sigma\varepsilon = \frac{1}{2}\frac{\sigma^2}{E} \tag{2}$$

In the case of a beam in flexion, the normal stress can be expressed according to bending moment $M_f$:

$$\sigma_{xx} = \frac{M_f}{I_{Gz}} y \tag{3}$$

In order to make the normal stress uniform along the beam, a first conceivable solution is to apply a constant moment. This situation is simple to simulate but difficult to realize in practice. However, for a common actuation configuration using a localized force or displacement (as in the case described in this paper), the natural variation in the bending moment can be balanced by a variation of the equilibrium between quadratic inertia $I_{Gz}$ and the distance to the point from the neutral line $y$. The following section will explore this solution.

### 3.2. Energy release rate evaluation with beam theory

The objective in this section is to set up an analytical model based on the beam theory that will ensure the optimization of the substrate shape by modifying locally its thickness for making the evolution of the energy release rate uniform along it. Execution time has to be relatively short compared to a 2D-FEM model in order to enable fast parametric optimization of substrate thickness profiles. Moreover, the objective is also to develop a proper code that does not require licenses.

An analytical half beam model is thus formulated. The two conditions previously introduced are simulated: clamped boundary conditions and pinned boundary conditions. The objective is to achieve energy computation in order to be able to compute the energy release rate $G$ between two different fracture states. The half beam is divided into a given number of sections and computations are made for each section in order to compute each variable along the beam axis. Computations are made according to two loops: an axial position loop that makes the computation for each section along the axis; and a"temporal" loop, that recreates a beam geometry according to the propagation of the crack. As explained previously, it is assumed that after adhesive debonding, the ice block loses all its strain energy. Therefore, the adhesive crack is modelled by removing the corresponding ice block from the computation (Fig. 7).

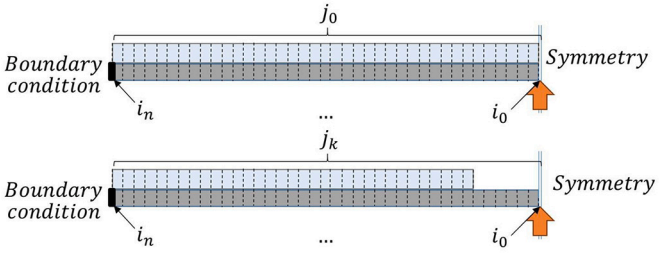


**Fig. 7.** Example of two different fracture states (sound and with $k$ crack length).

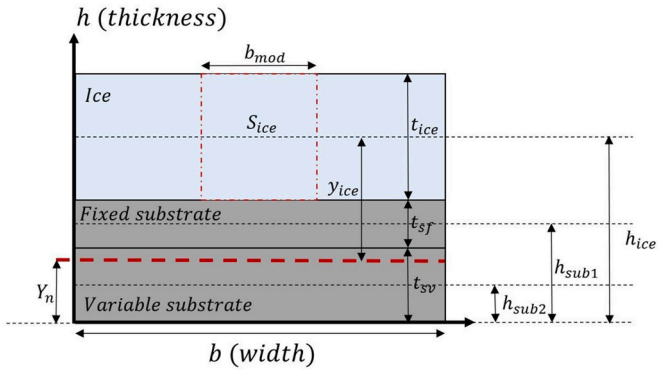


**Fig. 8.** Beam section $i_k$.

The beam section can be divided into three layers (Fig. 8). On the top of the beam, there is the ice layer, then there is the fixed thickness substrate layer defined by the minimum structural thickness needed (to ensure that the optimization will not completely erase the substrate) and lastly, the variable thickness substrate layer. The model is defined by a matrix of dimension [$i$,$j$] where $i$ represents the axial position of the section and $j$ represents the length of the crack. For each state of the crack $j$, the ice thickness is set to 0 to simulate the shedding of the ice block.

The first step in establishing the model involves computing the neutral line of the beam. The difference in the Young's modulus of the two materials must be taken into account. To compute the neutral line position with the mono-material formula, a bi-material ratio $n_{\text{young}} = \frac{E_s}{E_i}$ (with $E_i$ the Young modulus of the ice and $E_s$ the Young modulus of the substrate) is used to re-scale the width and consequently the axial surface of one of the materials according the materials stiffness. The modified width of the ice is defined by:

$$b_{\text{mod}} = \frac{b_{\text{real}}}{n_{\text{young}}} \tag{4}$$

The beam neutral line position is then computed with the following formula:

$$Y_n = \frac{\sum_{1:l}^{k} (S_k \cdot h_k)}{\sum_{1:l}^{k} S_k} \tag{5}$$

where $S_k$ is the axial surface of the $k$ layer among $l$ total layers and $h_k$ the absolute height of the neutral line of the $k$ layer.

Then, the second step in establishing the model is computing the quadratic inertia of each section of the beam using Huygens theorem for each layer:

$$I_G = \sum_{1:l}^{k} \left( \frac{b_k t_k^3}{12} + S_k y_k^2 \right) \tag{6}$$

where $t_k$ is the thickness of layer $k$ and $y_k$ the distance between the neutral line height of layer $k$ and the beam section's neutral line height $Y_n$.

From there, it is possible to link the vertical displacement $U_y$ of a beam section with the bending moment $M_f$, the Young Modulus $E$ and the quadratic inertia $I_G$ of the beam section:

$$\frac{d^2 U_y(x)}{dx^2} = \frac{M_f(x)}{E I_{Gz}(x)} \tag{7}$$

In the pinned case, for the first half of the beam, the bending moment is given by:

$$M_f(x) = \frac{-Fx}{2} \tag{8}$$

The boundary conditions give $U_y(0) = 0$ on the pinned side and $\dot{U}_y\left(\frac{L}{2}\right) = 0$ on the symmetry side, which makes it possible to compute the vertical displacement of each section of the beam by solving (7)

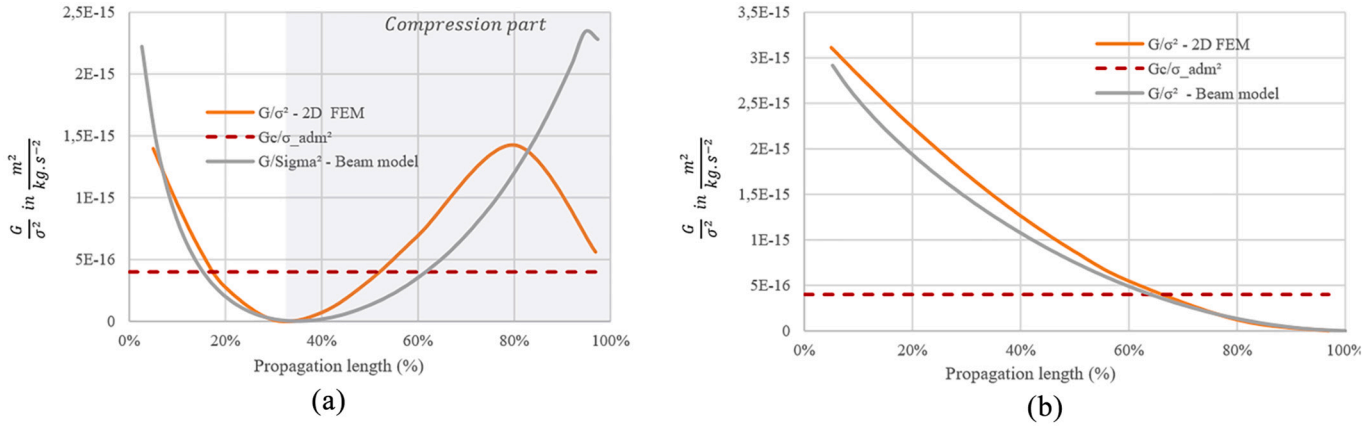


**Fig. 9.** 2D FEM computations and beam model computations of the energy release rate for clamped (a) and pinned conditions (b).

numerically.

In the clamped case, the problem is hyper-static. For the first half of the beam, the bending moment is given by:

$$M_f(x) = M_0 - \frac{Fx}{2} \tag{9}$$

The boundary conditions give $U_y(0) = 0$ and $\dot{U_y}(0) = 0$ on the clamped side and $\dot{U}_y\left(\frac{L}{2}\right) = 0$ on the symmetry side. With this, the vertical displacement of each section of the beam is computed using (7) and solving the hyper-static problem by computing $M_0$.

It is now possible to compute the maximum normal stresses (at the distance $h_{max}$ from the neutral line of the section) with:

$$\sigma_{xx} = -\frac{M_f}{I_G} \cdot h_{max} \tag{10}$$

energy density $w_e$ is computed with Eq. (2) and therefore the strain energy of the half beam for a given fracture length $j$ with:

$$E_j = \int_0^{L/2} \int_0^{h_t} \int_0^{b} w_e dx dy dz \tag{11}$$

$$E_j = \frac{1}{2E} \int_0^{L/2} \int_0^{h_t} \int_0^{b} \frac{M_f^2(x)}{I_G^2(x)} y^2 dx dy dz \tag{12}$$

where $b$ is the width of the real sample.

The computation of the energy according to the length of crack $j$ is used to compute the energy release rate:

$$G_j = \frac{1}{b} \frac{E_j - E_{j+1}}{x_j - x_{j+1}} \tag{13}$$

Finally, Fig. 9 shows the results of the $G/\sigma^2$ criterion versus the length of the crack computed using a 2D FEM model and the beam model.

Fig. 9 confirms that the analytical beam model and the 2D-FEM model with ANSYS give similar results for the computation of the ratio $G/\sigma^2$ for both clamped and pinned conditions. Thus the analytical beam model which gives results more quickly, requires less numerical resources and is simpler to implement will be used for the parametric optimization problem.

### 3.3. Definition of the optimization problem

Computations of the energy release rate performed for the adhesive crack propagation along the regular beam length show that, for the early stages of the propagation, $G$ value is significantly higher than the critical value. Therefore, the idea is to reduce the rate of decay of the energy release rate in order to keep the energy release rate level higher than critical level $G_c$ over an extended length in order to perform de-icing over a larger surface. To this end, it is proposed in this paper to modify the shape of the substrate by changing its thickness along the beam. The objective here is to determine a substrate profile minimizing the decrease of the energy release rate while keeping its value higher than the critical value.

#### 3.3.1. First optimization loop

Knowing the descending behavior of the function $G(l_f)$ according to the fracture length $l_f$, a first idea is to minimize the difference between the maximum and minimum values of $G(l_f)$ computed on the surface to be protected from ice:

$$\underset{\text{thickness}}{minimize} \; max\left(G(l_f)\right) - min\left(G(l_f)\right) \tag{14}$$

The numerical resolution of min/max problems using local quantities can, however, be difficult. Therefore, preference was given to using an objective function obtained by computing mean values of the whole surface which facilitates the convergence of the solution.

In the clamped configuration, solving (7) and using the bending moment formula (9) was used for computing the moment at the clamped side $M_0$. In this problem, while the thickness is being modified, the moment $M_0$ changes to fulfill the displacement and rotation conditions at the beam tips. This can be shown simply in the case of a bi-clamped beam with a constant section and a centered punctual load. Indeed, in this configuration, the moment in the clamp is defined as:

$$M_0 = k \cdot \frac{F \cdot L}{8} \tag{15}$$

where $k$ is equal to 1 in the case of a constant section beam. When $k$ is equal to 1, the beam's inflexion point is in the middle of the half beam. This means that half of the length of the beam is in traction and the other half is in compression. In order to achieve delamination, the ice needs to be loaded in traction (Marbœuf et al., 2020). Therefore, to increase the delamination area, it is important to extend the traction part and reduce the compression part. This can be done by moving the beam's inflexion point towards the clamp. As the slope of the bending moment remains constant whether the section is constant or not (Eq. (9)), the only way to move the inflexion point is to lower the $M_0$ value and consequently the $k$ value. Therefore, minimizing $k$ is one of the objectives for extending the delamination area. However, minimizing $k$ is not a sufficient condition to fulfill the propagation. The $G$ level also needs to remain above the critical value. Therefore, to achieve efficient de-icing, the objective is also to maximize $G$ values. It is important to consider the structural health of the substrate, however, and therefore the $G/\sigma^2$ criterion is used. Once again, the criterion is only studied on the frozen part loaded in traction as the part loaded in compression does not allow fracture propagation (Marbœuf et al., 2020).

From this analysis, it is possible to identify two objectives:

$$\underset{\text{thickness}}{minimize}\, k \tag{16}$$

and,

$$\underset{\text{thickness}}{maximize}\frac{G}{\sigma^2} \tag{17}$$

A combination of both functions is made in order to solve the problem with a single objective optimization algorithm. The final cost function of the minimization problem is defined as:

$$\underset{\text{thickness}}{minimize}\left\{\frac{< k >}{< \frac{G}{\sigma^2}.\frac{\sigma^2_{adm}}{G_c} >}\right\} \tag{18}$$

The criterion is multiplied by $\sigma^2_{adm}/G_c$ to normalize the value and facilitate convergence. The mean value is used for both terms.

In the pinned configuration, the bending moment is constant and the whole upper part of the beam is loaded in traction. There is therefore only one term in the pinned model cost function:

$$\underset{\text{thickness}}{minimize}\left\{\frac{1}{< \frac{G}{\sigma^2}.\frac{\sigma^2_{adm}}{G_c} >}\right\} \tag{19}$$

Numerical constraints are now integrated to the optimization problem to ensure that the fracture mechanism is respected. The fracture path is defined assuming the 3-step fracture mechanism of Fig. 4.

The initiation of the cohesive fracture at the ice surface can only occur if.

the ratio of $\sigma icesym/\sigma maxsub$ is greater than $\sigma admice/\sigma admsub$. If this is not the case, failure in the substrate material will occur before crack initiation in the ice. The following normalized constraint is therefore defined to ensure that the initiation of cohesive fractures occurs.

$$C_1 = \frac{\sigma_{ice_{sym}}}{\sigma_{max_{sub}}}.\frac{\sigma_{adm_{sub}}}{\sigma_{adm_{ice}}} - 1 > 0 \tag{20}$$

Then, as the load increases, the adhesive cracks need to be propagated at the interface without having other cohesive crack initiations that would disturb the fracture mechanism under study (the usefulness of subsequent cohesive crack for concrete application is not investigated in this paper). It is possible to ensure that there will not be any other cohesive crack initiation by having a structure that imposes a decrease in the tensile stress in the ice as the adhesive fracture extends. The following normalized constraint is therefore defined:

$$C_2 = \frac{\sigma_{ice}[i]}{\sigma_{ice}[i+1].\epsilon} - 1 > 0 \tag{21}$$

where $\epsilon$ is the minimum required slope of the tensile stress.

Theoretically, this constraint should not be necessary as the tensile stress in the ice should be naturally descending for a fixed ice thickness (bending moment is the greatest in the middle of the beam). In practice, due to unavoidable uncertainties encountered when working on ice samples, a minimum slope needs to be imposed to ensure that local irregularities in the ice thickness will not trigger additional cohesive cracks.

### 3.3.2. *Second optimization loop*

The mass of the structure is then optimized by running a second optimization loop. The goal of this loop is to use previous loop results to find a compromise between propagation efficiency and the additional mass due to the increase in the substrate thickness. The objective function is modified to include mass concerns and a new constraint is added (24) to ensure that the new result is not too far from the optimum obtained previously. The second optimization loop is run with an initial thickness corresponding to the optimized thickness of the first loop.

For the clamped configuration, the cost function is defined as:

$$\underset{\text{thickness}}{minimize}\left\{\frac{\text{mass}}{\text{mass}_{\max}} + < k >\right\} \tag{22}$$

For the pinned configuration, the cost function is simply:

$$\underset{\text{thickness}}{minimize}\left\{\frac{\text{mass}}{\text{mass}_{max}}\right\} \tag{23}$$

The constraint $C_3$ is defined to control drift from the previous computed minimum, where $Obj_0$ is the numerical value of the cost function obtained with the first optimization loop, and $Coef_{optim}$ the coefficient used to specify the allowed loss of efficiency in the propagation length:

$$C_3 = \left((1 + Coef_{\text{optim}}).Obj_0.\left\{\frac{< \frac{G}{\sigma^2}.\frac{\sigma^2_{\text{adm}}}{G_c} >}{< k >}\right\}\right) - 1 > 0 \tag{24}$$

In the case of pinned configuration, $k$ is considered equal to 1.

Figs. 10 and 11 show the optimized substrate shape for both clamped and pinned conditions and the associated criterion value according to the length of the adhesive fracture. The $\epsilon$ value is selected to impose a decrease of 1% in the stress level every 1 mm of beam length. An allowed drift of 20% from the first loop optimum is used to reduce the mass.

Results can be compared to those obtained for uniform aluminum substrates. Using the optimized design, the length of the propagation is in- creased.

For the clamped configuration:

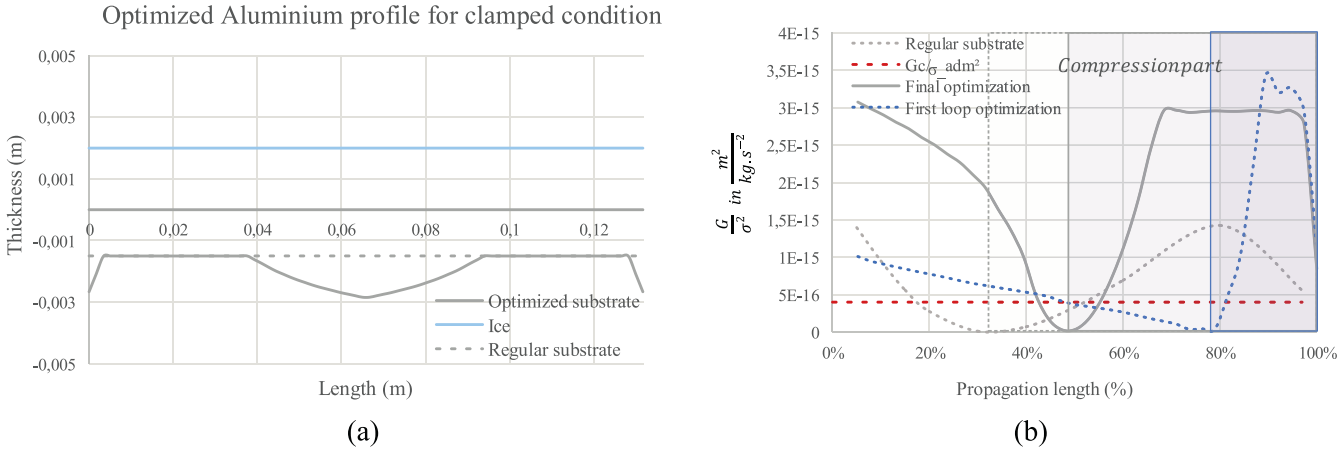


**Fig. 10.** Substrate shape for clamped configuration optimization and associated energy release rate criterion curves, including both optimization steps.

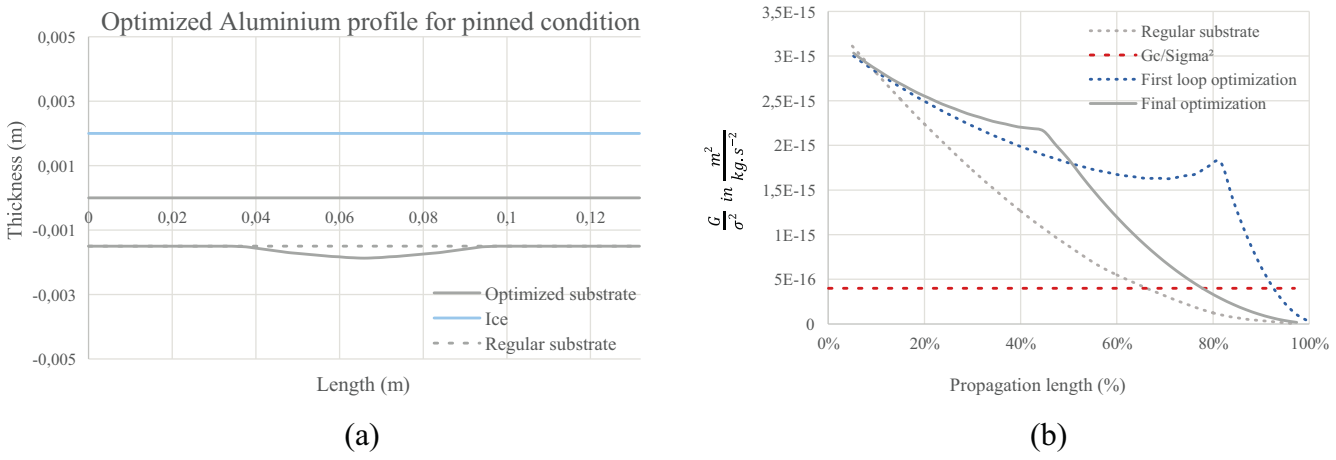


**Fig. 11.** Substrate shape for pinned configuration optimization and associated energy release rate criterion curves, including both optimization steps.

The practical length ($G_c = 1$) increased from 18% to 46% (156% increase) with the first optimization loop.

- The theoretical length increased from 30% to 50% (67% increase).
- Mass optimization reduced the mass by 55% compared to the first optimization loop while keeping a propagation length very close to the first result (45% compared to 46%). The final mass was 50% heavier than the regular substrate.

For the pinned configuration:
The practical length ($G_c = 1$) increased from 60% to 91% (52% increase) with the first optimization loop.

- The theoretical length remains at 100%
- Mass optimization reduced the mass by 30% compared to the first optimization loop but the propagation length was reduced to 77% (28% increase). The final mass is 6% heavier than the regular substrate.

A compromise can be made between mass optimization and propagation length. This can be taken into account directly by modifying the $Coef_{optim}$ value. Fig. 12 shows how the gain in mass and the gain in propagation length can be balanced to achieve various performances. This shows the range of configurations that can be realized using the methodology proposed in this article.

## 4. Experimental verification

A 3-point bending test bench was designed to verify the numerical results computed in the previous sections. The test bench enables the clamping of the sample on both ends and a vertical displacement is imposed in the middle of the plate using an electric cylinder from Newport (TRA25PPD series) (Fig. 14). The cylinder displacement in monitored and controlled with great precision (µm) and the actuator can deploy a maximum force of 60 N. The test bench is installed in a freezing environment (−20 °C) to recreate the ice on the sample. After cleaning the adhesive surface with alcohol, a controlled amount of demineralized water is sprayed until getting more or less a 2 mm-thick ice layer which corresponds to the case considered for the theoretical computations. Silicone plates are placed at the start of the freezing process next to the clamps to ensure that the ice only bonds to the sample and not to the clamps and removed after a few minutes while the sample is left in the freezer to complete the freezing. Two different samples were tested. The reference sample is a simple, 1.5 mm-thick aluminum plate, 40 mm in width and 130 mm in length (between the clamps). The aluminum used is 2017 A (AU4G). According to the thickness profile computed in this paper, a second sample is machined (Fig. 13), with the same width, length and material as the first regular sample. For both samples, the adhesive surface is polished using sandpaper (Grit P4000), an equivalent average roughness of 0.50 µm is measured at the ice/substrate interface.

The main objective of this experiment is to confirm that the

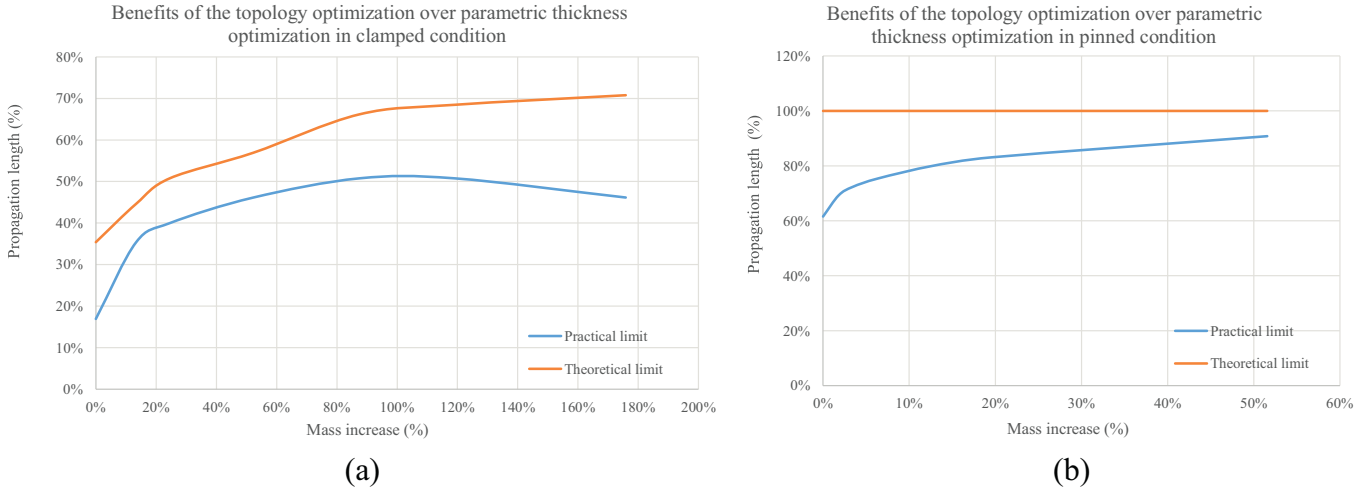


**Fig. 12.** Propagation length of the adhesive fracture according to the mass increase of the substrate for both configurations.

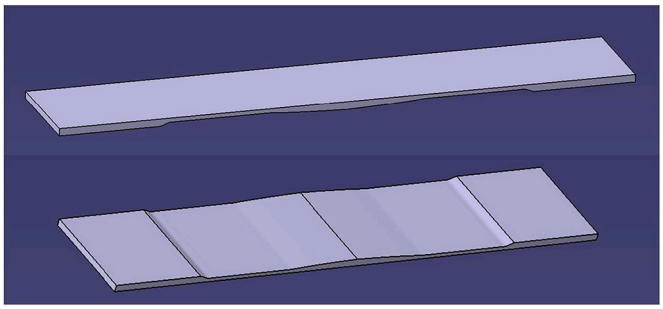

**Fig. 13.** 3D CAD model of the clamped optimized sample.

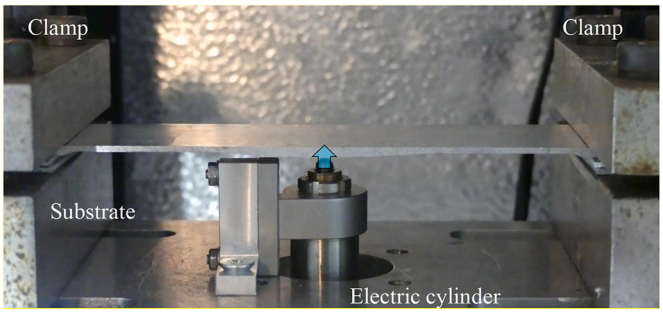


**Fig. 14.** Photography of the 3 point bending bench with the optimized substrate.

optimized substrate extends the delamination length at the ice/substrate interface. For both samples, the displacement corresponding to a 50 MPa stress in the substrate is computed in order to get the same stress loading for both structures during the tests. By reaching the critical stress of 50 MPa in the substrate, the propagation length should correspond to the practical limit defined in the previous sections, if the $G_c$ of the ice corresponds to the 1 J/m$^2$ assumed for the numerical models. Moreover, by taking a limit value as low as 50 MPa, the elasticity of the substrate is maintained through the tests, removing all potential plasticity effect on the experiment results.

For the regular substrate, a stress of 50 MPa is reached for a 0.33 mm vertical displacement at the center of the plate. For the optimized design, the displacement can be increased to 0.45 mm before reaching the critical stress.

Ten tests were carried out for each configuration. The ice thickness was measured in three different locations along the plate length using a vernier caliper. An average thickness is retrieved from these measurements. The thicknesses are not identical for all samples but remain in the range of 2 mm with an average value of 2.64 mm. Moreover, because of the ice generation process used, the ice thickness is not constant across the surface. However, beside of the unavoidable meniscus shape on the edges of the sample and the dome shape in the center, the ice appears relatively homogeneous with a standard deviation of the thickness of 12.5% and a maximum deviation of 21.5% considering all the samples generated. According to the numerical results displayed on Fig. 10, in the case of the regular substrate, the length of the propagation should be on average 18% of the plate if the $G_c$ of the ice is equal to 1 J/m$^2$. In the case of an over estimation of this critical value, the propagation could extend to the maximal theoretical limit, 30%. For the optimized design, the average propagation should be around 40% of the substrate length and at maximum, 50%. These are the value numerically predicted in the case of an homogeneous 2 mm thick ice of 920 kg/m3 density with a Young's modulus of 9.3 GPa and a critical energy release rate of 1 J/m$^2$.

Figs. 15 and 16 show an example of pictures from the regular substrate experiment. Fig. 17 shows an equivalent view of the result for the optimized substrate. For both configurations the fracture mechanism expected was observed, even if the cohesive crack is not centered because of the non homogeneity of the ice deposit. In some cases, for the optimized substrate, two cohesive cracks were observed on the edges of the optimized area. In fact, high tensile stress were observed to be located at the end of the optimized area but remained under the maximum tensile stress, located at the center of the plate. Once again, because of the non homogeneity of the ice and the possible imperfections of the test bench, the criterion might have not been respected for

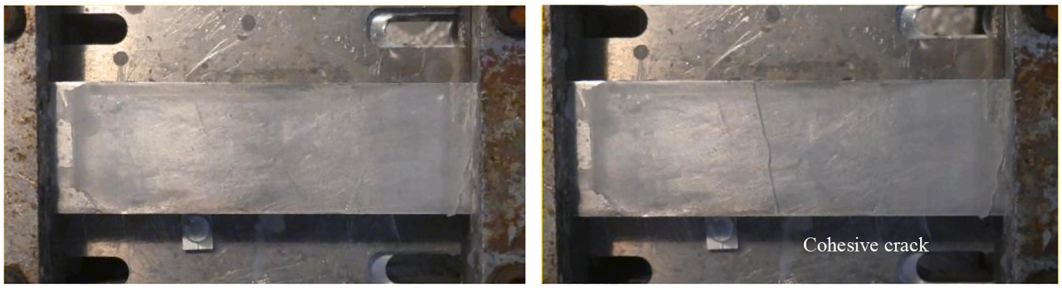


**Fig. 15.** Top view of the regular sample covered by ice (a) and the appearance of the cohesive crack (b).

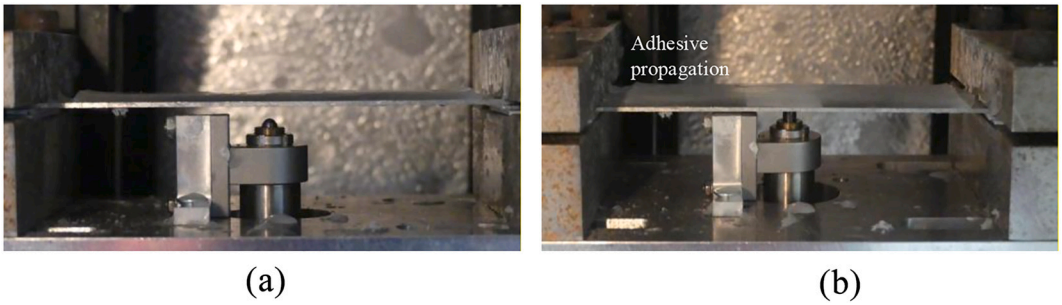


**Fig. 16.** Side view of the regular sample covered by ice (a) and adhesive crack (b).

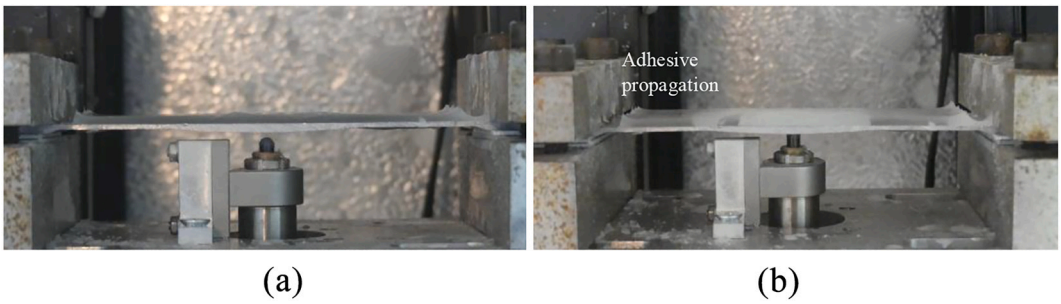


**Fig. 17.** Side view of the optimized sample covered by ice (a) and adhesive crack (b).

every test, leading to the appearance of two outer cracks. The results from the experiment are plotted in Fig. 18. An increase in the propagation length is observable for the optimized substrate regardless of the variation in the ice thickness of the tested samples. Extending from 24% on average for the regular substrate to 46% on average for the optimized one, the magnitude of the propagation length matches with the computations, which verifies the parametric optimization methodology and the analytical beam model. The results present some scattering which is however acceptable in the authors opinion. On the regular substrate, the mean deviation of the propagation length is 11% and the maximum deviation is 25%. On the optimized substrate, the scattering is diminished with a standard deviation of 6% and a maximum deviation of 12%. This can be explained by the increase of the propagation length, making the measurement error relatively lower. Also, as shown in Fig. 10, the delta between the practical and the theoretical length is reduced, leading to a less important influence of the adhesion properties on the experimental propagation length measurement. Despite the scattering of the measurements inherent in experiments with ice, the results appear to confirm the theoretical expectations.

A last experiment was performed on each substrate to verify that increasing the displacement over the critical value did not imply a significant increase in the adhesive propagation and that the theoretical maximum value was reached. For the regular substrate, the displacement was increased to 0.50 mm and the adhesive crack length reached 37% of the plate length, thus only a small increase compared to the adhesive crack length of 35% for a vertical displacement of 0.15 mm. In the case of the optimized substrate, the adhesive crack length reached 50% for 1 mm displacement, slightly more than the 43% for the 0.45 mm displacement. This last experiments show that the theoretical maximum length was reached (Fig. 20) and that, even for a displacement on the regular beam greater than the one imposed to the optimized substrate, the propagation length would still remain lower for the non-optimized substrate (Fig. 19).

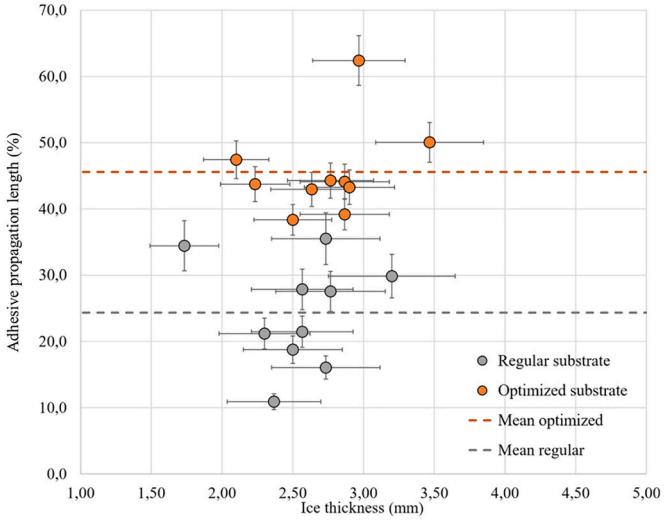


**Fig. 18.** Propagation length according to the substrate type and the ice thickness.


**Fig. 19.** Side view of the regular sample for a 0.15 mm long displacement (a) and a 0.50 mm long displacement (b).

(a) (b)

**Fig. 20.** Side view of the regular sample for a 0.45 mm long displacement (a) and a 1 mm long displacement (b).

## 5. Mass minimization thanks to topology optimization

Parametric optimization shown the benefits of the modification of the substrate shape on the adhesive crack propagation. In this section, a different method is used to extend de reshaping freedom to more than only one dimension (thickness). Contrary to the parametric optimization presented, topology optimization provides a complete freedom in reshaping the substrate. Using such method could provide better minimization of the additional mass while maintaining the practical delamination length obtained in the previous section (Fig. 10 for the clamped configuration and Fig. 11 for the pinned configuration). The objective of this section is to investigate the potential benefits of a more complex substrate geometry in term of crack propagation length and mass.

### 5.1. Problem formulation

Fig. 21 displays the configuration, applied loads and material's parameters. 2D plain strain geometry is considered. As stated before, fracture occurs instantaneously compared to the loading rate and a quasi-static framework is adopted. Each state then corresponds to a configuration with a given adhesive fracture length on which static linear elastic finite element computation is performed. All classical fields, such as displacement, strain, stress or elastic energy, are available everywhere in the computational domain for each state. For the half-model of the study case, the fracture propagates approximately every 6.5 mm leading to 10 discretization points on the adhesive interface.

The protected zone length is fixed at 91% for the pinned configuration and 48% for the clamped configuration, according to Figs. 10 and 11.

The computational domain shown in Fig. 21 is discretized into approximately 615,000 element cells. In each element cell $c$, Young's modulus $E_c$ and stress $\sigma_c$ are degraded according to the modified Solid Isotropic Material with Penalization (SIMP) approach (Sigmund, 2001; Andreassen et al., 2011)

$$E_c = E_{min} + \rho_c^p (E_{\text{mat}} - E_{min}) \tag{25}$$

$$\sigma_c = \rho_c^q \sigma_{mat} \tag{26}$$

where $E_{mat}$ is the material Young's modulus, $E_{min} = 10^{-4}$ allows an invertible stiffness matrix to be kept, $p = 3$ and $q = 1.5$ are penalization parameters (Sigmund, 2001; Andreassen et al., 2011; Holmberg et al., 2013).

The optimization problem is now formulated as follows.

$$\min_{\rho} \quad \frac{m^r}{G_N^s}$$

$$\text{submitted to:} \begin{cases} \dfrac{G_{i+1} - G_i}{G_i} \leq -0.05 & i = 0, \ldots, N \\ \dfrac{G_c}{\left(\sigma_{adm}^{VM}\right)^2} - \dfrac{G_N}{\left(\sigma_N^{VM}\right)^2} \leq 0 \\ 0 \leq \rho \leq 1 \end{cases} \tag{27}$$

where $m$ is the mass proportion, $i$ denotes the state number, $G_c/(\sigma_{adm}^{VM})^2$ the critical value introduced in section 2.4 and $N$ is the maximum state number given the fixed protected length. With 10 points on the adhesive interface, the fixed protected length of 91% yields the value $N = 10$ for the pinned configuration and a surface protection of 47% yields $N = 5$ for the clamped configuration. The objective is weighted thanks to parameters $r = 2$ and $s = 1$. The mass is minimized while the last energy release rate of the protected zone $G_N$ is maximized. Note that emphasis is put on the mass in the objective with the weighted parameters $r$ and $s$.

The problem formulation is completed by the definition of constraints. The first constraint sorts all the energy release rates along the adhesive interface on the protected zone $G_0 > G_1 > \ldots > G_N$ and imposes a maximum slope of 5% locally. This constraint ensures that the fracture path is followed and is therefore the counterpart of constraints $C_1$ and $C_2$

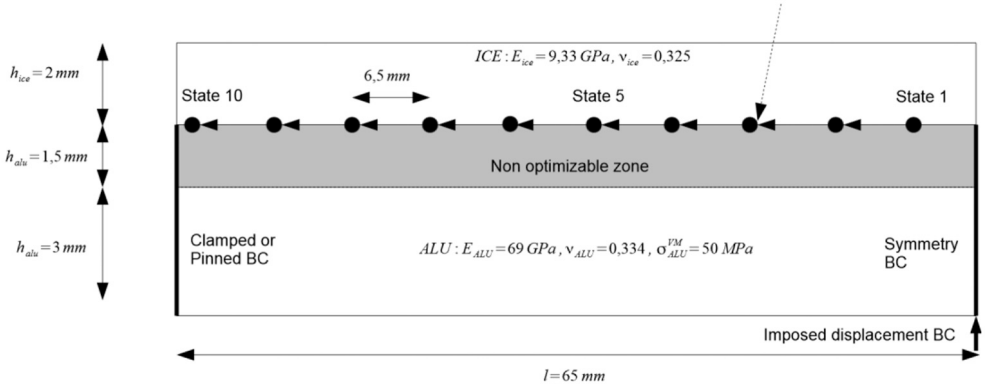


**Fig. 21.** Configuration used for topology optimization. The material's parameters are displayed. Each state corresponds to a static computation given a fracture delamination length.

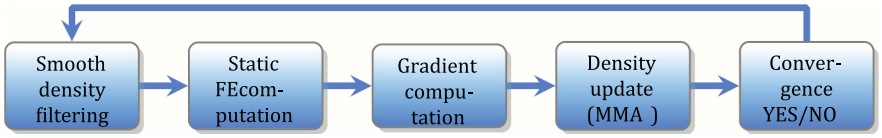


**Fig. 22.** Flowchart of the topology optimization algorithm.

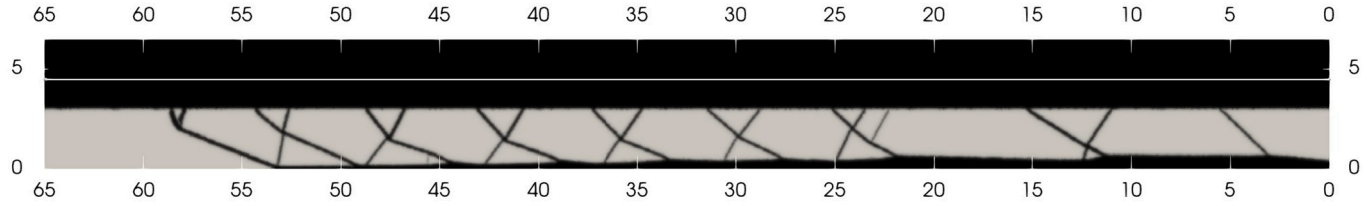


**Fig. 23.** Optimized design for the pinned configuration. The blank line indicates the substrate-ice interface.

in Eqs. (20) and (21). For computational considerations, here the energy release rate replaces the stress in $C_1$ and $C_2$. Stresses need very fine meshes to be well-resolved, especially in this case where only local stresses are of interest at each discretization point. This assumption can be made as proportionality is shown between $\sigma^2$ and $G$ (Palanque et al., *2021*). The second constraint is the criterion introduced in section 2.3 to ensure fracture propagation without damaging the substrate. For this purpose, the quantity $\sigma_N^{VM}$ represents the maximum Von-Mises stress value within the substrate at state $N$.

The computation of energy release rate $G$ at each state is performed according to

$$G = \frac{1}{\delta\ell}\int_0^{\delta\ell} \frac{1}{2}\left[k_n < [[\boldsymbol{u}]]_n >_+^2 + k_\tau [[\boldsymbol{u}]]_\tau^2\right] d\ell \tag{28}$$

where $\delta\ell \simeq 1$ mm is a virtual fracture length. Eq. (28) is the elastic energy locally stored in the adhesive interface between 0 (starting from the discretization point) and $\delta\ell$. The adhesive interface is modelled by elastic microscopic bonds (Frémond, 1987; Bennani et al., 2016; Marbœuf et al., 2020) and takes the form of a potential spring energy of stiffness $k_n$ and $k_\tau$. The normal value $k_n = 9.48 \times 10^{12}$ Pa/m is related to more common adhesive material parameters available in the literature through a pure traction test [Marbœuf et al., 2020, Section 4]. These parameters are the critical energy release rate $G_c = 1$ J/m$^2$ and the critical stress $\sigma_c \simeq 1.41$ MPa, which are displayed in Fig. 21. Tangential stiffness $k_\tau$ is taken such that contribution is divided by 10 compared to Mode I [Marbœuf et al., 2020, Section 4], i.e. $k_\tau = k_n/10$. Displacement jump $[[u]]$ across the adhesive interface is split into normal and tangential components: $<[[\boldsymbol{u}]\|_n>_+$ denotes the positive part of the normal displacement jump, i.e. the normal traction (Mode I fracture), and $[[\boldsymbol{u}]]_\tau$ the tangential part, i.e. shear (Mode II fracture). Note that this separation makes it possible to remove the normal compression from the energy release rate: compression does not participate in adhesive fracture (Miehe et al., 2010).

Problem (27) is now solved using classical techniques that exists in the literature. A smoothing filter (Lazarov and Sigmund, 2011) reduces mesh-dependency and improves convergence. Length parameter $R = 5.0$ is chosen in the numerical results, leading to smoothing over approximately 5 cells. No Black & White filter (Russ and Waisman, 2019) is used to remove intermediate values $0 < \rho < 1$. Such filters break the first constraint, which is overly sensitive to local modifications of intermediate densities. The discrete $L^k$-norm with $k = 4$ approximates the maximum value of the Von-Mises stress within the substrate. All element values of $\sigma_N^{V\,M}$ are sorted and dispatched into 3 clusters to improve the approximation of the maximum value without increasing $k$ (Holmberg et al., *2013*). The first constraint becomes a vectorial constraint with 3 components, but accuracy on the maximum VonMises stress is greatly improved. Finally, the Method of Moving Asymptotes (MMA) (Svanberg, 1987) solves the problem (27). Sensitivities with respect to the design $\rho$ required by MMA are computed with the Adjoint Method. See (Russ and Waisman, 2019; Holmberg et al., 2013) for an example of adjoint sensitivity computations.

Fig. 22 displays the flowchart of the topology optimization algorithm.

### 5.2. *Results analysis and mass impact assessment*

Figs. 23 and 24 respectively show the optimal design for the pinned and the clamped configurations obtained from topology optimization. Both designs are similar, and as in parametric optimization, increase the thickness of the substrate in the center as seen in section 3.3. The main difference with parametric optimization is the presence of branches allowing reducing the mass of the substrate. The thickness remains constant over the large part of the protected zone and begins to decrease only on the last 7 mm. Note also that the thickness of the main branch decreases with the adhesive fracture length when moving away from the center of the beam. Consequently, stiffness also decreases together with energy release rates along the interface in order to respect the first constraint of (27). The major contribution of topology optimization compared to parametric optimization is that most of the mass is removed inside the optimized design. Only reinforcement branches remain where discretization points are placed on the adhesive interface. Again, it makes it possible to locally maximize the stiffness at these points, and consequently to increase the energy release rate. The optimal structure


**Fig. 24.** Optimized design computed for the clamped configuration. The blank line indicates the substrate-ice interface.

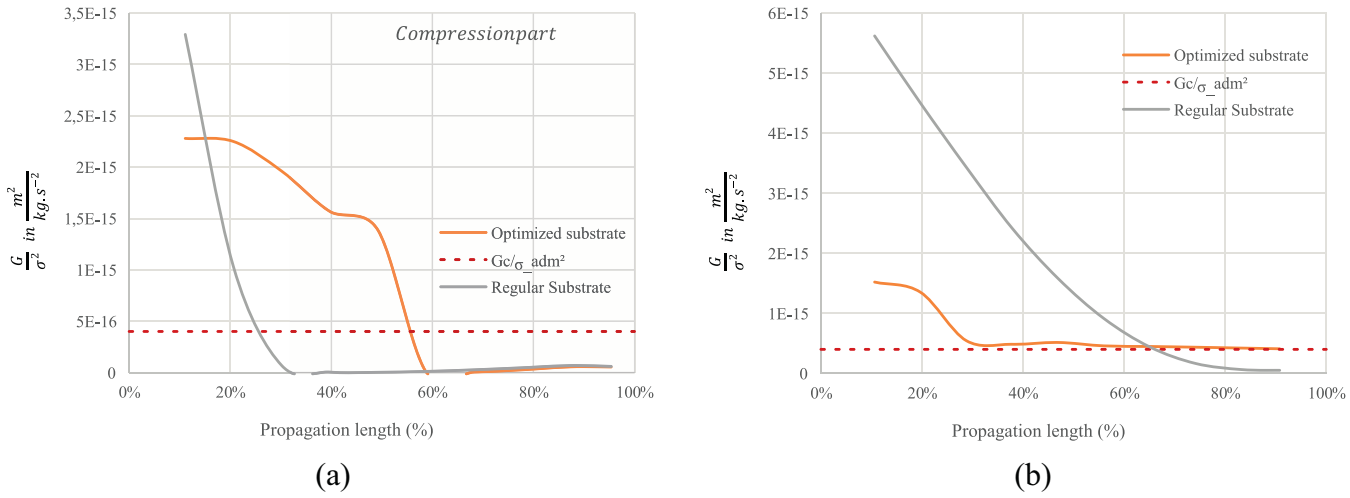


**Fig. 25.** Energy release rate criterion curves computed with topology optimization for the pinned and clamped configurations.

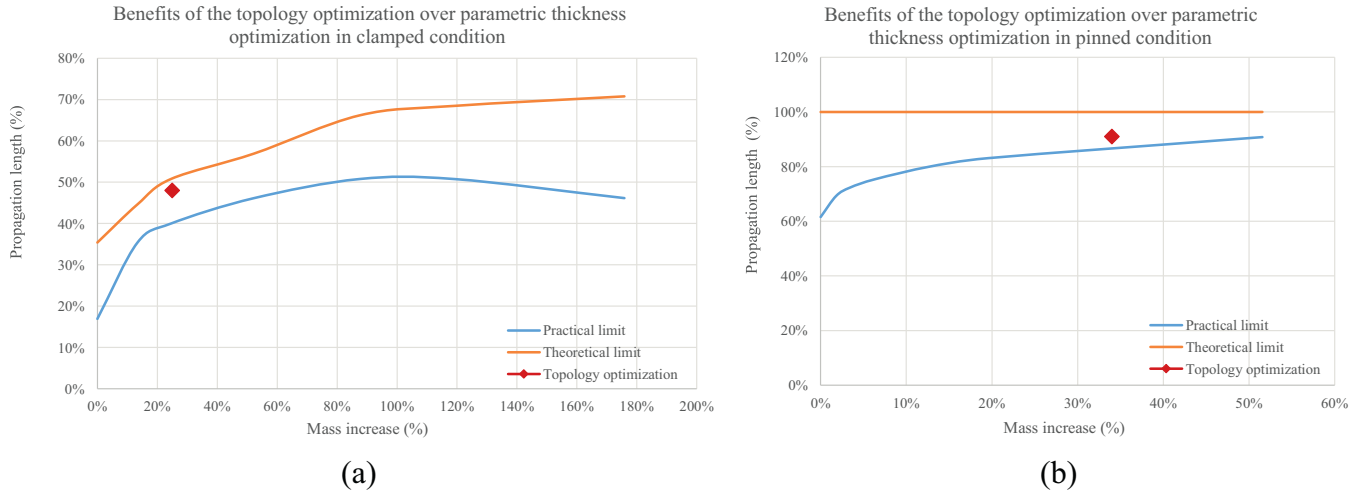


**Fig. 26.** Propagation length of the adhesive fracture according to the mass increase of the substrate for pinned and clamped configuration: Fig. 12. Topology optimization results are added.

here thus depends on the discretization performed for the adhesive interface. In the end, the substrate mass is reduced up to 60% compared to parametric optimization while keeping the same protection.

Figs. 25 and 26 both show the benefits of topology optimization compared to the parametric results. Fig. 25 shows that:

delamination was improved from 76% to 91% for the pinned configu- ration

- delamination was improved from 26% to 48% for the clamped configuration
- Performances were maintained with topology optimization, while the additional mass weight was reduced by 60% (Fig. 26)

Fig. 26 shows that the topology optimization enables to approach the theoretical limit with a reduced mass impact.

### 5.3. *Experimental verification of the topology optimization*

As for the previous experimental verification, the objective is to test the clamped design shown in Fig. 24on the test bench developed for the parametric optimization sample. However, because of the complexity of the matter arrangement of the substrate, the manufacturing of the sample is difficult or even impossible to achieve through standard manufacturing process. The only two conceivable solutions are the EDM (electrical discharge machining) and the 3D metal printing. However, in both cases, the cavities and the branches dimensions are way below the accuracy of the processes and therefore, the design needs to be adapted to enable its manufacturing. The 3D metal printing is eventually selected for cost, delay and tolerance concerns.

Fig. 27 shows the half model of the modified design to be manufactured.

The prototype is printed in Titanium instead of Aluminum, which increases the strength of the substrate to failure. However it also modified the Young's modulus of the material and therefore the arrangement of the substrate does not match as well with the geometry defined by the topology optimization. During the manufacturing process, small deflections occur in the material because of thermal effects.

**Fig. 27.** Modified design for manufacturing purposes.

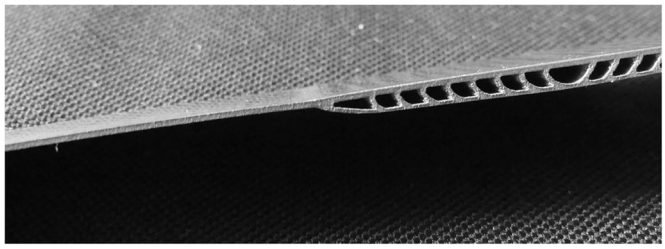

**Fig. 28.** Deflection on the manufactured substrate.

**Fig. 29.** Non plan surface of the substrate highlighted after polishing.

In fact, at the contact areas between the branches, the material shrinks, damaging the substrate surface. Because of the branches thinness, the deflections lead to a non plan substrate which is highlighted after attempting to polish the surface (Figs. 28 and 29). Because of all these undesired effects, the improvement of the adhesive propagation is not clearly observed and the fracture mechanism required for the study is not obtained. These manufacturing issues highlighted the fact that the manufacturing limits are not negligible in this kind of optimization and that the manufacturing process should be taken into account prior to the optimization in order to define proper constraints to ensure the feasibility of the design.

## 6. Conclusion

This article proposes to increase the efficiency of mechanical energy release rate based de-icing by modifying the substrate on which the ice accumulates. Two methods are proposed. The first method based on a simplified analytical beam model is used to achieve the parametric optimization on the substrate thickness. To go further, a second method based on the topology optimization of the substrate with a 2D finite element model was developed. Computations and experiments carried out on a beam showed that optimization of the substrate profile is efficient in increasing the mechanical de-icing range.

By optimizing the substrate thickness along the beam, the adhesive fracture propagation range is extended for both clamped and pinned conditions.

The numerical results for the study case of this article show a gain of up to 150% for the propagation length for the beam in clamped conditions, and a gain of up to 50% for the pinned conditions. The beam in clamped conditions optimized thanks to parametric optimization was compared to a regular substrate using a 3 point bending test bench. The experiment confirmed the expected results from the numerical analysis, showing the benefit of the parametric optimization on the adhesive crack length.

However, results show that a compromise is to be made between propagation length and overall structure mass. Indeed,the additional mass due to the increase in the substrate thickness rises with the ability of the substrate to propagate the crack. In order to achieve high fracture propagation length and keep the mass as low as possible, the method based on topology optimization promises good performance. For the case under study, the additional mass obtained with parametric optimization was reduced by >60% (clamped condition) or 30% (pinned condition) using topology optimization, while maintaining de-icing performance. However, the experimental verification was not possible for the topology optimization as the substrate appeared to be not feasible. This highlighted the fact that, for this kind of optimization, the manufacturing limits should be identified prior to the optimization and included in the numerical model as constraints to permit the realization of the sample.

Nevertheless, the studies performed on a simple plate geometry with static loading have shown encouraging results. Implementing modal displacement computations would be an interesting way to extend the static study of substrate optimization to resonant de-icing system applications. In the case of topology optimization, it could be interesting to investigate the modification of numerical parameters (such as weights $r$ and $s$ or the number of discretization points on the adhesive interface) or geometrical parameters. These parameters are fixed a priori and their modifications could indeed lead to different designs, possibly more optimal. Finally, applying the substrate optimization method to more realistic geometries such as airfoil should be of prime interest in the development of low consumption electro-mechanical de-icing systems for the aeronautical industry.

## Declaration of Competing Interest

None.

## Appendix A. Supplementary data

Supplementary data to this article can be found online at https://doi.org/10.1016/j.coldregions.2022.103641.

## References


Akl, W., El-Sabbagh, A., Al-Mitani, K., Baz, A., 2009. Topology optimization of a plate coupled with acoustic cavity. Int. J. Solids Struct. 46 (10), 2060–2074 special Issue in Honor of Professor Liviu Librescu. doi:10.1016/j.ijsolstr.2008.05.034. URL https://www.sciencedirect.com/science/article/pii/ S0020768308002096.

Anderson, T.L., 2005. Fracture mechanics: fundamentals and applications, 3rd edition. Taylor & Francis, Boca Raton, FL.

Andreassen, E., Clausen, A., Schevenels, M., Lazarov, B.S., Sigmund, O., 2011. Efficient topology optimization in matlab using 88 lines of code. Struct. Multidiscip. Optim. 43 (1), 1–16.

Andrews, E.H., Lockington, N.A., 1983. The cohesive and adhesive strength of ice. J. Mater. Sci. 18 (5), 1455–1465. https://doi.org/10.1007/BF01111965. URL http://link.springer.com/10.1007/BF01111965.

Bauchau, O.A., Craig, J.I., 2009. Euler-Bernoulli beam theory. In: Bauchau, O.A., Craig, J.I. (Eds.), Structural Analysis, Solid Mechanics and Its Applications. Springer Netherlands, Dordrecht, pp. 173–221. https://doi.org/10.1007/978-90-481-2516-6_5. URL doi:10.1007/978-90-481-2516-6_5.

Bennani, L., Villedieu, P., Salaun, M., 2016. A mixed adhesion–brittle fracture model and its application to the numerical study of ice shedding mechanisms. Eng. Fract. Mech. 158, 59–80. https://doi.org/10.1016/j.engfracmech.2016.02.050. URL http:// www.sciencedirect.com/science/article/pii/ S0013794416300765.

Budinger, M., Pommier-Budinger, V., Napias, G., Costa da Silva, A., 2016. Ultrasonic ice protection systems: analytical and numerical models for architecture tradeoff. J. Aircr. 53 (3), 680–690. https://doi.org/10.2514/1.C033625. URL http://arc.aiaa.org/doi/10.2514/1.C033625.

Budinger, M., Pommier-Budinger, V., Bennani, L., Rouset, P., Bonaccurso, E., Dezitter, F., 2018. Electromechanical resonant ice protection systems: analysis of fracture propagation mechanisms. AIAA J. 56 (11), 4412–4422. https://doi.org/10.2514/1.J056663. URL https://arc.aiaa.org/doi/10.2514/1.J056663.

Budinger, M., Pommier-Budinger, V., Reysset, A., Palanque, V., 2021. Electromechanical resonant ice protection systems: energetic and power considerations. AIAA J. 59 (7), 2590–2602 publisher: American Institute of Aeronautics and Astronautics eprint: https://doi.org/10.2514/1.J060008. doi:10.2514/1.J060008. URL. https://doi.org/10.2514/1.J060008.

Druez, J., Nguyen, D., Lavoie, Y., 1986. Mechanical properties of atmospheric ice. Cold Reg. Sci. Technol. 13 (1), 67–74. https://doi.org/10.1016/0165-232X(86)90008-X. URL https://linkinghub.elsevier.com/retrieve/pii/ 0165232X8690008X.

D. N. Ely, J. H. Macarchenia, Pneumatic deicer, uS Patent 4,779,823 (Oct. 25 1988).

Frémond, M., 1987. Adhérence des solides. Journal de mécanique théorique et appliquée 6 (3), 383–407.

Golovin, K., Dhyani, A., Thouless, M., Tuteja, A., 2019. Low–interfacial toughness materials for effective large-scale deicing. Science 364 (6438), 371–375.

Holmberg, E., Torstenfelt, B., Klarbring, A., 2013. Stress constrained topology optimization. Struct. Multidiscip. Optim. 48 (1), 33–47.

Huang, X., Tepylo, N., Pommier-Budinger, V., Budinger, M., Bonaccurso, E., Villedieu, P., Bennani, L., 2019. A survey of icephobic coatings and their potential use in a hybrid coating/active ice protection system for aerospace applications. Prog. Aerosp. Sci. 105, 74–97. https://doi.org/10.1016/j.paerosci.2019.01.002. URL https://www.sciencedirect.com/science/article/pii/ S0376042118301167.

R. B. Ingram, G. W. Codner, J. J. Gerardi, Electro-magnetic expulsion de-icing system, uS Patent 5,782,435 (Jul. 21 1998).

Lawn, B.R., 1993. Fracture of brittle solids. In: 2nd Edition, Cambridge solid state science series. Cambridge University Press, Cambridge; New York.

Lazarov, B.S., Sigmund, O., 2011. Filters in topology optimization based on helmholtz-type differential equations. Int. J. Numer. Methods Eng. 86 (6), 765–781.

Leguillon, D., 2002. Strength or toughness? a criterion for crack onset at a notch. Eur. J. Mech. A/Solids 21 (1), 61–72.

Marbœuf, A., Bennani, L., Budinger, M., Pommier-Budinger, V., 2020. Electromechanical resonant ice protection systems: numerical investigation through a phase-field mixed adhesive/brittle fracture model. Eng. Fract. Mech. 230, 106926. https://doi.org/10.1016/j.engfracmech.2020.106926. URL https://www.sciencedirect.com/science/article/pii/ S0013794419311014.

Martin, E., Vandellos, T., Leguillon, D., Carr`ere, N., 2016. Initiation of edge debonding: coupled criterion versus cohesive zone model. Int. J. Fract. 199 (2), 157–168.

O. Meier, D. Scholz, A handbook method for the estimation of power requirements for electrical de-icing systems, DLRK, Hamburg 31.

W. Meng, Y. Guo, Experimental Study on Mechanical Properties of Ice 5.

Miehe, C., Hofacker, M., Welschinger, F., 2010. A phase field model for rate-independent crack propagation: robust algorithmic implementation based on operator splits. Comput. Methods Appl. Mech. Eng. 199 (45), 2765–2778. https://doi.org/10.1016/j.cma.2010.04.011. URL http://www.sciencedirect.com/science/article/pii/ S0045782510001283.

Moir, I., Seabridge, A., 2011. Aircraft Systems: Mechanical, Electrical, and Avionics Subsystems Integration, 52. John Wiley & Sons.

Niemann, H., Morlier, J., Shahdin, A., Gourinat, Y., 2010. Damage localization using experimental modal parameters and topology optimization. Mech. Syst. Signal Process. 24 (3), 636–652. https://doi.org/10.1016/j.ymssp.2009.10.022. URL https://www.sciencedirect.com/science/article/pii/ S0888327009003707.

Palanque, V., Budinger, M., Pommier-Budinger, V., Bennani, L., Delsart, D., 2021. Electro-mechanical Resonant Ice Protection Systems: Power requirements for fractures initiation and propagation, in: AIAA AVIATION 2021 FORUM. AIAA AVIATION Forum, American Institute of Aeronautics and Astronautics. https://doi.org/10.2514/6.2021-2651. URL. https://arc.aiaa.org/doi/10.2514/6.2021-2651.

Parent, O., Ilinca, A., 2011. Anti-icing and de-icing techniques for wind turbines: Critical review. Cold Reg. Sci. Technol. 65 (1), 88–96 anti-Icing and De-Icing Techniques. doi:10.1016/j.coldregions.2010.01.005. URL https://www.sciencedirect.com/science/article/pii/ S0165232X10000108.

J. J. Petrovic, Review Mechanical properties of ice and snow 6.

Pommier-Budinger, V., Budinger, M., Rouset, P., Dezitter, F., Huet, F., Wetterwald, M., Bonaccurso, E., 2018. Electromechanical resonant ice protection systems: initiation of fractures with piezoelectric actuators. AIAA J. 56 (11), 4400–4411. https://doi.org/10.2514/1.J056662. URL https://arc.aiaa.org/doi/10.2514/1.J056662.

Raj, L.P., Yee, K., Myong, R.S., 2020. Sensitivity of ice accretion and aerodynamic performance degradation to critical physical and modeling parameters affecting airfoil icing. Aerosp. Sci. Technol. 98, 105659. https://doi.org/10.1016/j.ast.2019.105659. URL https://www.sciencedirect.com/science/article/pii/ S127096381931805X.

Reich, A., Scavuzzo, R., Chu, M., 1994. Survey of mechanical properties of impact ice. In: in: 32nd Aerospace Sciences Meeting and Exhibit, American Institute of Aeronautics and Astronautics, Reno,NV,U.S.A. https://doi.org/10.2514/6.1994-712. URL http://arc.aiaa.org/doi/.

Russ, J.B., Waisman, H., 2019. Topology optimization for brittle fracture resistance. Comput. Methods Appl. Mech. Eng. 347, 238–263. https://doi.org/10.1016/j.cma.2018.12.031. URL https://www.sciencedirect.com/science/article/pii/ S0045782518306303.

Shi, Z., Kang, Z., Xie, Q., Tian, Y., Zhao, Y., Zhang, J., 2020. Ultrasonic deicing efficiency prediction and validation for a flat deicing system. Appl. Sci. 10 (19), 6640.

Shinkafi, A., Lawson, C., 2014. Enhanced method of conceptual sizing of aircraft electro-thermal de-icing system. Int. J. Mech. Aerospace, Indust. Mech. Eng. 8 (6), 1069–1076.

Sigmund, O., 2001. A 99 line topology optimization code written in matlab. Struct. Multidiscip. Optim. 21 (2), 120–127.

Sommerwerk, H., Horst, P., 2017. Analysis of the mechanical behavior of thin ice layers on structures including radial cracking and de-icing. Eng. Fract. Mech. 182, 400–424.

Sommerwerk, H., Luplow, T., Horst, P., 2020. Numerical simulation and validation of electro-impulse de-icing on a leading edge structure. Theor. Appl. Fract. Mech. 105, 102392.

Svanberg, K., 1987. The method of moving asymptotes—a new method for structural optimization. Int. J. Numer. Methods Eng. 24 (2), 359–373.

Tryde, P. (Ed.), 1980. Physics and Mechanics of Ice: Symposium Copenhagen, August 6–10, 1979, Technical University of Denmark, Springer Berlin Heidelberg, Berlin, Heidelberg. https://doi.org/10.1007/978-3-642-81434-1. URL http://link.springer.com/10.1007/978-3-642-81434-1.

Vercillo, V., Karpen, N., Laroche, A., Guillén, J.A. Mayen, Tonnicchia, S., de Andrade Jorge, R., Bonaccurso, E., 2019. Analysis and modelling of icing of air intake protection grids of aircraft engines. Cold Reg. Sci. Technol. 160, 265–272. https://doi.org/10.1016/j.coldregions.2019.01.012. URL https://www.sciencedirect.com/science/article/pii/ S0165232X18304415.

Villeneuve, E., Volat, C., Ghinet, S., 2020. Numerical and experimental investigation of the design of a piezoelectric de-icing system for small rotorcraft part 1/3: development of a flat plate numerical model with experimental validation. Aerospace 7 (5), 62. https://doi.org/10.3390/aerospace7050062. URL. https://www.mdpi.com/2226-4310/7/5/62.

E. Villeneuve, C. Volat, S. Ghinet, Numerical and experimental investigation of the design of a piezoelectric de-icing system for small rotorcraft part 3/3: numerical model and experimental validation of vibration-based de-icing of a flat plate structure, Aerospace 7 (5) 54. doi:10.3390/aerospace7050054. URL https://www.mdpi.com/2226-4310/7/5/54.

E. Villeneuve, C. Volat, S. Ghinet, Numerical and experimental investigation of the design of a piezoelectric de-icing system for small rotorcraft part 2/3: investigation of transient vibration during frequency sweeps and optimal piezoelectric actuator excitation, Aerospace 7 (5) 49. doi:10.3390/aerospace7050049. URL https://www.mdpi.com/2226-4310/7/5/49.

Zargham, S., Ward, T.A., Ramli, R., Badruddin, I.A., 2016. Topology optimization: a review for structural designs under vibration problems. Struct. Multidiscip. Optim. 53 (6), 1157–1177.

Zehnder, A.T., 2013. Griffith Theory of Fracture. In: Wang, Q.J., Chung, Y.-W. (Eds.), Encyclopedia of Tribology. Springer US, Boston, MA, pp. 1570–1573. https://doi.org/10.1007/978-0-387-92897-5_259. URL https://doi.org/10.1007/978-0-387-92897-5_259.